Equilibrium Electrodeformation of a Spheroidal Vesicle in an AC Electric Field

H. Nganguia and Y.-N. Young
Department of Mathematical Sciences,
New Jersey Institute of Technology, Newark, New Jersey 07102, USA
(Dated: September 2, 2013)

Abstract

In this work we develop a theoretical model to explain the equilibrium spheroidal deformation of a giant unilamellar vesicle (GUV) under an alternating current (AC) electric field. Suspended in a leaky dielectric fluid the vesicle membrane is modeled as a thin capacitive spheroidal shell, and the equilibrium vesicle shape results from balancing the mechanical forces from the viscous fluid, the elastic membrane and the imposed electric field. Our spheroidal model predicts a deformation-dependent transmembrane potential, and is able to capture large deformation of a vesicle under an electric field. Detailed comparison against both experiments and small-deformation (quasi-spherical) theory showed that the spheroidal model gives better agreement with experiments in terms of the dependence on fluid conductivity ratio, permittivity ratio, vesicle size, electric field strength and frequency. The spheroidal model allows for an asymptotic analysis on the crossover frequency for a prolate vesicle to cross over to an oblate shape (or vice versa), and comparisons show the spheroidal model gives better agreement with experimental observations.

I. INTRODUCTION

The electro-deformation and electro-dynamics of vesicles (closed pure lipid bilayer membranes) have been a paradigm for understanding how a biological cell behaves under an electric field. Vesicles are known to change their shape depending on the frequency of the imposed alternating current (AC) electric fields and the mismatch in fluid conductivities[1–4]. Changes in vesicle orientation, dielectrophoresis and electrorotation have also been observed. Under direct current (DC) electric fields, both vesicles and biological cells tend to undergo large deformations with aspect ratios reaching ten. The permeabilization of vesicles membranes using electric fields has also generated a lot of practical and modeling interest, especially in the biotechnology industry. Electroporation, the process of perforating the membrane by applying an (often DC) electric field, has been proposed as a method for delivering molecules into living organisms[5–13]. Most recently electroporation has been used for measurements of various properties of the cell membranes[13,14].

The earliest theories of vesicle electro-deformation[15,16] were based on minimizing the total surface energy, consisting of the membrane mechanical energy (from tension and bending) and electrical energy (from Maxwell stresses). These models focus on conductivity ratio ≈ 1, and as a result the models were only able to predict prolate shape. Extension of these models[17,18] allow for large conductivity mismatch and predict the various shapes observed experimentally[4], even though poor quantitative agreement with the experiments is found. Hyuga *et al.* [19,20] proposed the first theory (to our knowledge) beyond the surface energy minimization approach. Sadik *et al.* [21] modified this approach to model the deformation of spheroidal vesicles under strong strong electric fields.

Vlahovska *et al.* [22] proposed a perturbative method to study the dynamics and deformation of a nearly-spherical vesicle subject to weak AC electric fields. Assuming small asphericity, they used the transmembrane potential for a dielectric spherical shell in AC fields in the analyses. The small-deformation results are in qualitative agreement with experiments in terms of shape elongation and the transition frequency between prolate and oblate vesicle. Yet the small-deformation theory does not apply to vesicles subjected to moderate and strong electric fields, where deformations are well beyond the nearly spherical shape[1]. Zhang *et al.* [23] proposed a spheroidal model to study the transient dynamics of highly deformed vesicles under strong DC electric fields. Assuming that vesicles remain spheroidal under a slowly varying DC electric field, which is well supported by experimental findings in[1,21,24], their spheroidal results are in quantitative agreement with experimental data[23] in terms of the vesicle aspect ratio and its response to an electric pulse.

In this article, we extend the spheroidal model in[23] to study the equilibrium electro-deformation of a vesicle in AC fields. Unlike the dynamical approach for solving the transmembrane potential in[23], we develop a model for the equilibrium transmembrane potential for a spheroidal dielectric shell in AC fields. The article is organized as follows: In § II we formulate the problem. In § II A we present the transmembrane potential for a spheroidal dielectric shell, we then derive the governing equation in § II B. Our findings are summarized in § III: We first present a comparison between the spheroidal model and the small deformation theory for a prolate vesicle; in § III A we consider the dependence of vesicle de-

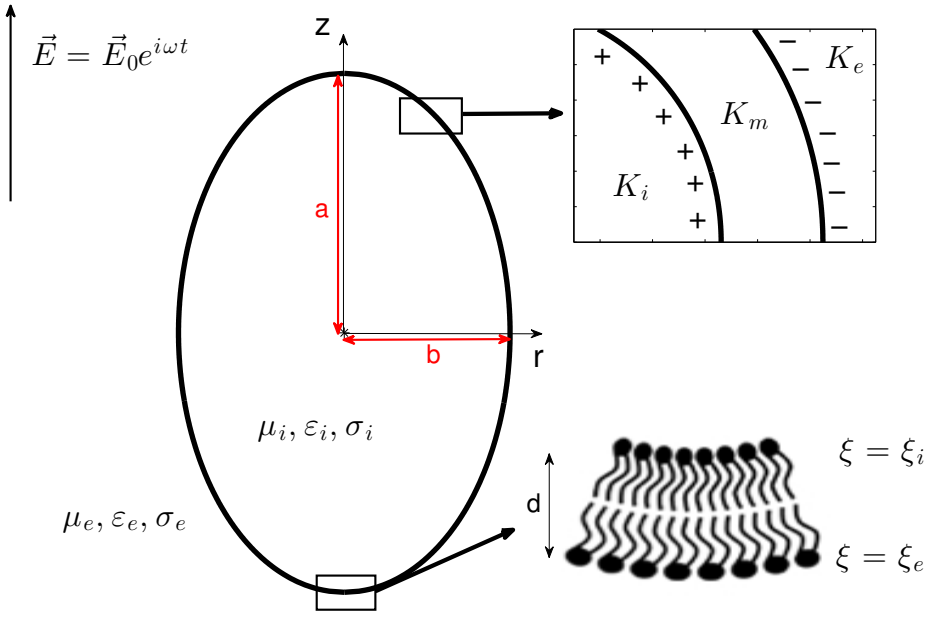

FIG. 1. Illustration of a vesicle suspended in a leaky dielectric fluid. The typical membrane thickness, $d = 5$ nm. The bottom inset shows the lipid bilayer structure of the membrane, and the top inset shows the three dielectric spheroidal shells with electric impedance defined in equation 9.

formation, transmembrane potential and electric stresses on the field frequency. In § III B, we show the predictions, as well as comparison with experiment for the shape elongation and transition frequency.

II. PROBLEM FORMULATION

Figure 1 illustrates a spheroidal vesicle enclosing an interior dielectric fluid $(\mu_i, \varepsilon_i, \sigma_i)$ suspended in another dielectric fluid with $(\mu_e, \varepsilon_e, \sigma_e)$. μ, ε and σ are the fluid viscosity, dielectric permittivity and conductivity, respectively, and the subscript denotes interior (i) or exterior (e) fluids. Typical values of the fluid viscosity (larger than 10^{-3} Pa s) and vesicle size (several μm's) indicate that the fluid inertia are negligible, consequently the flow velocity in both interior and exterior fluids is governed by the incompressible Stokes equations

$$\mu_j \nabla^2 \boldsymbol{u}_j = \nabla p_j, \qquad \nabla \cdot \boldsymbol{u}_j = 0, \tag{1}$$

where p is the fluid pressure, $\boldsymbol{u}$ is the fluid velocity with the subscript $j = e$ for exterior fluid or $j = i$ for interior fluid. The boundary conditions for the velocity are $\boldsymbol{u} = 0$ in the far-field, and $\boldsymbol{u} = \frac{d\boldsymbol{x}}{dt}$ on the vesicle membrane, with $\boldsymbol{x}$ denoting the vesicle membrane location. The balance of stresses on the membrane gives

$$\boldsymbol{n} \cdot [\![\mathbf{T} + \mathbf{S}]\!] = \boldsymbol{\tau}^{mem}, \tag{2}$$

where $[\![f]\!] \equiv f_e - f_i$ denotes the difference between exterior and interior and $\boldsymbol{n}$ is the outward normal unit vector on the membrane. $\mathbf{T} = -p\mathbf{I} + \mu\left((\nabla \boldsymbol{u})^T + \nabla \boldsymbol{u}\right)$ is the hydrodynamic stress with $\mathbf{I}$ the identity tensor, and $\mathbf{S} = \varepsilon \vec{\mathbf{E}}\vec{\mathbf{E}} - \frac{\varepsilon}{2}\left(\vec{\mathbf{E}} \cdot \vec{\mathbf{E}}\right)\mathbf{I}$ is the Maxwell stress. The membrane traction (force density) consists of membrane tension and bending forces,

$$\boldsymbol{\tau}^{mem} = 2\sigma_h H \boldsymbol{n} - \kappa\left(4H^3 - 4KH + 2\nabla_s^2 H\right)\boldsymbol{n}, \tag{3}$$

where σ_h, κ, H and K are the membrane tension, bending rigidity, mean curvature and Gaussian curvature, respectively. The (homogenous) membrane tension is related to the excess area $\Delta \equiv \frac{A}{4\pi r_0^2} - 1$ as

$$\sigma_h = s_0 \exp\left[\frac{8\pi\kappa\Delta}{k_B T}\right], \tag{4}$$

where $s_0 = \sigma_0/(\kappa/r_0^2)$ is the dimensionless membrane tension.

The electric field is harmonic ($\vec{\mathbf{E}} = \vec{\mathbf{E}}_0 e^{i\omega t}$) and irrotational, which implies that $\vec{\mathbf{E}} = -\nabla\phi$ with ϕ the electric potential that satisfies the Laplace equation both inside and outside the vesicle

$$\nabla^2 \phi_j = 0. \tag{5}$$

Across the membrane the electric potential has a jump

$$\phi_i - \phi_e = \Delta\phi, \tag{6}$$

due to the capacitive nature of the vesicle membrane. The induced charges on the two sides of membrane cause a discontinuity in the displacement vector

$$[\![\varepsilon \vec{\mathbf{E}} \cdot \mathbf{n}]\!] = Q(\omega, t), \tag{7}$$

where Q is the induced charge density. If we neglect the effects of charge convection along the membrane, the electric current conservation at the interface gives

$$[\![\sigma \vec{\mathbf{E}} \cdot \mathbf{n}]\!] = -\frac{dQ}{dt} \approx -\frac{\partial Q}{\partial t}. \tag{8}$$

Substituting equation 7 into equation 8 yields the continuity condition

$$[\![-K\nabla\phi \cdot \mathbf{n}]\!] = 0, \quad K_j = \sigma_j + i\omega\varepsilon_j, \tag{9}$$

where the dielectric properties are characterized by the complex electrical impedance. j can be i, m, and e, referring to interior, membrane, and exterior of the vesicle. σ_j, ε_j and ω are the conductivity, permittivity and electric field frequency, respectively. For the vesicle's impedance $K_m = G_m d + iC_m d$, where G_m and C_m are the membrane conductance and capacitance.

We non-dimensionalize the governing equations by scaling length to r_0, time to the charging time $t_c = \varepsilon_e/\sigma_e$, the electric potential to $E_0 r_0$, bending force and membrane tension to κ/r_0^2 and electric stresses to $\varepsilon_e E_0^2$. For example the resultant dimensionless complex conductivities are given by

$$K_e = \frac{1}{x} + i\frac{\omega}{x}, \quad K_i = \frac{\sigma_r}{x} + i\frac{\omega\varepsilon_r}{x}, \quad K_m = \frac{\sigma_m}{\sigma_e x} + i\omega\frac{\varepsilon_m}{\varepsilon_e x} \tag{10}$$

where the conductivity and permittivity ratios are defined as $\sigma_r = \frac{\sigma_i}{\sigma_e}$ and $\varepsilon_r = \frac{\varepsilon_i}{\varepsilon_e}$. $x = \frac{d}{r_0}$ is the dimensionless thickness. σ_m and ε_m are the membrane conductivity and permittivity, respectively.

A. Transmembrane potential

In the leaky dielectric model the bulk charges are assumed to neutralize instantaneously, leaving induced charges on the interface between fluids of mismatched dielectric constant (such as electric conductivity). Because the membrane is impermeable, the induced surface charges accumulate on either side of the vesicle, giving rise to an electric potential jump across the membrane. In the past studies of vesicles subjected to ac electric fields[22,25] the transmembrane potential for a spherical shell is often used[26–28]. However the transmembrane potential depends on the geometry of the vesicle, and even small deviations from an initial spherical shape may induce noticeable changes in the potential jump[29].

Analytical studies on the induced transmembrane potential for spheroidal vesicles reveal that the membrane thickness is non-uniform due to the alignment of cell boundaries with spheroidal surfaces[30,31]. Klee and Plonsey[32] used numerical simulations to compute the spheroidal potential jump, while Gimsa *et al.* [29,33,34] devised a resistor-capacitor (RC) approach to determine the induced transmembrane potential. Later Konik[35] showed that small variations in the membrane thickness of spheroidal cells have no effects on the transmembrane potential.

Here we developed an analytical model of the transmembrane potential for a spheroidal shell in an ac electric field. The analytical solution is based on the truncated solution for the electric potential in the prolate spheroidal coordinates system (ξ, η), related to the cylindrical coordinates (r, z) by

$$z = c\xi\eta, \qquad r = c\sqrt{(\xi^2 - 1)(1 - \eta^2)}, \tag{11}$$

where $c \equiv \sqrt{b^2 - a^2}$ is the semi-focal length. Surfaces of constant $\xi \in [1, \infty)$ are spheroids while surface of constant $\eta \in [-1, 1]$ are hyperboloids. As such, the prolate vesicle surface is given by $\xi = \xi_0(t) \equiv \frac{a}{c}$.

The electric potential exists in three regions: interior (i), exterior (e), and the membrane (m), see the inset in figure 1. The transmembrane potential is obtained by solving Laplace equations in all three domains. We assume that the potential in each domain takes the truncated form[23,36–38]:

$$\phi_j = (\alpha_j \xi + \beta_j Q_1(\xi))\, \eta, \quad j = i, e, m, \tag{12}$$

where Q_1 is the Legendre polynomial of the second kind. α_j, β_j are obtained from the boundary conditions. Boundary conditions in the far-field and inside the vesicle yield $\alpha_e = -c$ and $\beta_i = 0$. The remaining coefficients $\beta_e, \alpha_m, \beta_m$, and α_i are similarly determined from boundary conditions on the membrane, see Appendix B. Substituting the coefficients in equation 12 we get :

$$\Delta\phi = \phi_i(\xi_i) - \phi_e(\xi_e) \equiv V_m \eta,$$

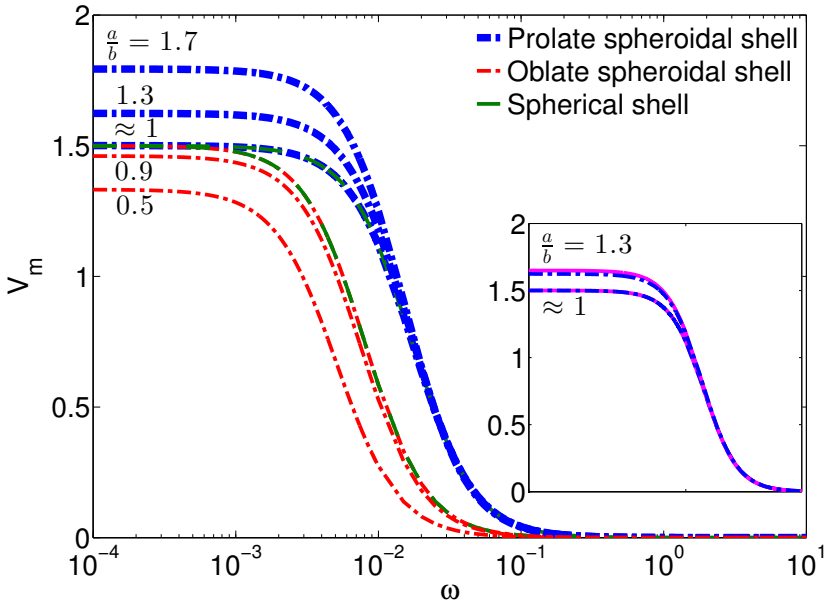

FIG. 2. Magnitude of transmembrane potential calculated from equation 13 for various aspect ratios. The thick (thin) dash-dotted lines are prolate, $\sigma_r = 1.5$ (oblate, $\sigma_r = 0.5$) predictions, and the dashed line is the spherical shell potential. The inset shows V_m for two prolate cases.

where $V_m = cF(\omega)/D(\omega)$ is the 'amplitude' of the potential, $D(\omega)$ is given by equation B7, and

$$F(\omega) = -K_e(Q_e - \xi_e Q'_e)\left((K_i - K_m)\xi_i Q_e + (-K_i\xi_e + K_m\xi_i)Q_i + K_m(\xi_e - \xi_i)\xi_i Q'_i\right). \tag{13}$$

The functions $Q_e \equiv Q_1(\xi_e), Q_i \equiv Q_1(\xi_i), Q'_e \equiv Q'_1(\xi_e), Q'_i \equiv Q'_1(\xi_i)$.

In figure 2 we provide a comparison of the transmembrane potential magnitude V_m between the spherical shell (dashed lines) and spheroidal shells (dash-dotted lines). Thick lines are for prolate with $\sigma_r = 1.5$, and thin lines are for oblate with $\sigma_r = 0.5$. At low frequencies, the spherical shell potential reaches the maximum value $V_m = 3/2$ while for the spheroidal shell V_m plateaus to a maximum that depends on the vesicle aspect ratio a/b: The larger the shape elongation, the larger the maximum transmembrane potential, in agreement with earlier findings about the dependence of the potential on shape[29]. We note that by solving the Laplace equation in each dielectric spheroidal shell, the η dependence in our spheroidal shell is the same as that in the spherical shell, while Gimsa *et al*'s model cannot capture the η dependence.

B. Electrohydrodynamic deformation

With the transmembrane potential for the spheroidal shell in equation 13, we can now compute the electric potentials in the interior and exterior of the vesicle as

$$\phi_e = \left(-c\xi + \alpha Q_1(\xi)\right)\eta e^{i\omega t}, \tag{14}$$

$$\phi_i = \beta\xi\eta e^{i\omega t}, \tag{15}$$

where α and β are obtained by satisfying the boundary conditions in equations 6 and 9:

$$\alpha = \frac{c\xi_0\left(K_r - 1\right) - K_r V_m}{K_r Q_1 - \xi_0 Q_1'}, \quad \beta = \frac{c\left(\xi_0 Q_1' - Q_1\right) - V_m Q_1'}{K_r Q_1 - \xi_0 Q_1'}, \tag{16}$$

with $K_r = \frac{K_i}{K_e}$. We write the electric field $\vec{\mathbf{E}}$ as the real part of $\mathcal{E}$: $\vec{\mathbf{E}} = \Re(\vec{\mathcal{E}}) = \frac{1}{2}\left(\vec{\mathcal{E}} + \vec{\mathcal{E}}^*\right)$ (where * denotes complex conjugation), and substitute it into the Maxwell stress[39]

$$\mathbf{S}(\omega) = \frac{\varepsilon}{4}\left(\vec{\mathcal{E}}\vec{\mathcal{E}}^* + \vec{\mathcal{E}}^*\vec{\mathcal{E}} - |\mathcal{E}|^2\mathbf{I}\right) + \frac{\varepsilon}{4}\left(\vec{\mathcal{E}}\vec{\mathcal{E}} + \vec{\mathcal{E}}^*\vec{\mathcal{E}}^* - \frac{1}{2}\left[\vec{\mathcal{E}}\cdot\vec{\mathcal{E}} + \vec{\mathcal{E}}^*\cdot\vec{\mathcal{E}}^*\right]\mathbf{I}\right). \tag{17}$$

In the above equation, the first group on the right hand side is the time-averaged Maxwell stress tensor, and the second group is the time-dependent (harmonic) terms. In the following we consider only the time-independent terms for equilibrium vesicle shapes.

We focus on the axi-symmetric incompressible fluid velocity field, which can be computed from a stream function ψ for both inside and outside the vesicle. The stream function satisfies the equation

$$(E^2)^2\psi = 0, \quad \text{with} \quad E^2 = \frac{1}{c^2\left(\xi^2 - \eta^2\right)}\left[(\xi^2 - 1)\frac{\partial^2}{\partial\xi^2} + (1 - \eta^2)\frac{\partial^2}{\partial\eta^2}\right]. \tag{18}$$

The general solution for the stream function takes the form[40,41]

$$\psi = g_0(\xi)G_0(\eta) + \sum_{n=2}^{\infty}\left(g_n(\xi)G_n(\eta) + h_n(\xi)H_n(\eta)\right), \tag{19}$$

where G_n and H_n are the Gegenbauer functions of the first and second kind, respectively. Detailed expressions of the functions g_n and h_n can be found in[40,41]. In this work we seek a solution truncated at leading order[23,36–38]

$$\psi_e = \left(A_3^1 H_1(\xi) + A_3^3 H_3(\xi)\right)G_3(\eta), \tag{20}$$

$$\psi_i = \left(B_3^3 G_3(\xi) + B_3^5 G_5(\xi)\right)G_3(\eta). \tag{21}$$

The four coefficients A's and B's, along with the shape function (ξ_0 for prolate or λ_0 for oblate), can be completely determined from the kinematic continuity condition, velocity boundary conditions and the stress balance (equation 2) on the membrane. Following the procedures in[23,42], we project the stress balance onto the corresponding velocities to close the system:

$$\int_{\xi=\xi_0(t)} u\left[[\![\mathbf{T}_{\xi\eta}]\!] + [\![\mathbf{S}_{\xi\eta}]\!]\right] ds = 0, \tag{22}$$

$$\int_{\xi=\xi_0(t)} v\left[[\![\mathbf{T}_{\xi\xi}]\!] + [\![\mathbf{S}_{\xi\xi}]\!] - \tau^{mem}\right] ds = 0. \tag{23}$$

In prolate spheroidal coordinates,

$$\mathbf{T}_{\xi\xi} = 2\mu\left(\frac{\partial v}{h_\xi \partial \xi} + \frac{u}{h_\xi h_\eta}\frac{\partial h_\xi}{\partial \eta}\right), \quad \mathbf{T}_{\xi\eta} = \mu\left(\frac{\partial (u/h_\eta)}{\partial \xi}\frac{h_\eta}{h_\xi} + \frac{\partial (v/h_\xi)}{\partial \eta}\frac{h_\xi}{h_\eta}\right), \tag{24}$$

$$\mathbf{S}_{\xi\xi} = \frac{\varepsilon}{4}\left(\mathcal{E}_\xi \mathcal{E}_\xi^* - \mathcal{E}_\eta \mathcal{E}_\eta^*\right), \quad \mathbf{S}_{\xi\eta} = \frac{\varepsilon}{4}\left(\mathcal{E}_\xi \mathcal{E}_\eta^* + \mathcal{E}_\eta \mathcal{E}_\xi^*\right), \tag{25}$$

where h_ξ and h_η are the scale factors in the spheroidal coordinates, $\mathcal{E}_\xi = -\frac{\partial \phi}{\partial \xi}$ and $\mathcal{E}_\eta = -\frac{\partial \phi}{\partial \eta}$ are the normal and tangential electric field. The excess area in equation 4 can be expressed in terms of ξ_0 as

$$\Delta = \frac{1}{2}\left(1 - \xi_0^{-2}\right)^{-2/3}\left[1 - \xi_0^{-2} + \sqrt{\xi_0^2 - 1}\arcsin\left(\xi_0^{-1}\right)\right] - 1. \tag{26}$$

The above derivation can be modified for the oblate case with appropriate transformation: $\xi \to i\lambda$ and $c \to -i\bar{c}$ with i the imaginary unit. Thus the oblate spheroidal coordinates (λ, η) are related to the cylindrical coordinates (r, z) as $z = \bar{c}\lambda\eta$, $r = \sqrt{(\lambda^2+1)(1-\eta^2)}$, with $\bar{c} \equiv \sqrt{b^2 - a^2}$ for $\lambda \in [0, \infty)$ and $\eta \in [-1, 1]$. Surfaces of constant λ are oblate spheroids while surfaces of constant η are hyperboloids. Consequently in oblate coordinates

$$E^2 = \frac{1}{c^2\left(\lambda^2 + \eta^2\right)}\left[(\lambda^2+1)\frac{\partial^2}{\partial \lambda^2} + (1-\eta^2)\frac{\partial^2}{\partial \eta^2}\right],$$

the electric potential coefficients and excess area take the following forms

$$\alpha = \frac{\bar{c}\lambda_0\left(K_r - 1\right) - K_r V_m}{K_r Q_1 - \lambda_0 Q_1'}, \quad \beta = i\frac{\left[\bar{c}Q_1 + \left(V_m - c\lambda_0\right)Q_1'\right]}{K_r Q_1 - \lambda_0 Q_1'}, \tag{27}$$

$$\Delta = \frac{1}{2}\left(1 + \lambda_0^{-2}\right)^{-2/3}\left[\sqrt{\lambda_0^{-2} + \lambda_0^{-4}} + \operatorname{arctanh}\left(\left(\lambda_0^2 + 1\right)^{-1/2}\right)\right] - 1. \tag{28}$$

Expressing all four coefficients $A's$ and $B's$ in terms of ξ_0 for prolate and λ_0 for oblate, we obtain the governing equation for the shape function as

$$\frac{d\chi}{dt} = \frac{\delta\left[\mathcal{Q}_N f_{21} + \mathcal{Q}_T \dfrac{f_{11}\left(\mu_r f_{22} + f_{23}\right)}{\mu_r f_{14} + f_{15}} - Ca_E^{-1}\left(\sigma_h f_{24} + f_\kappa\right)\right]}{\dfrac{2}{3}\left(\mu_r f_{25} + f_{26}\right)}, \tag{29}$$

$$\mathcal{Q}_N = \pm\frac{1}{2c^2}\left[2c^2 - 2c\tau_3\left(Q_1' + Q_1/\chi\right) + \left(\tau_3^2 + \tau_4^2\right)\left(Q_1'^2 + \left(Q_1/\chi\right)^2\right) - 2\left(\tau_1^2 + \tau_2^2\right)/\varepsilon_r\right], \tag{30}$$

$$\mathcal{Q}_T = \frac{1}{2c^2}\left[c^2\chi + \left(\tau_3^2 + \tau_4^2\right)Q_1 Q_1' - c\tau_3\left(Q_1 + \chi Q_1'\right) - \left(\tau_1^2 + \tau_2^2\right)\chi/\varepsilon_r\right], \tag{31}$$

where $\chi = \xi_0$ for prolate and λ_0 for oblate, and the symbols $\pm$ designate prolate $(+)$ or oblate $(-)$. $Ca_E = \frac{\varepsilon_e r_0^3 E_0^2}{\kappa}$ is the electric capillary number, and $\delta = \frac{t_c}{t_{EHD}}$ with $t_{EHD} = \frac{\mu_i}{\varepsilon_e E_0^2}$ the characteristic electro-hydrodynamics (EHD) timescale. The functions $f_{11} - f_{26}$, f_κ are given

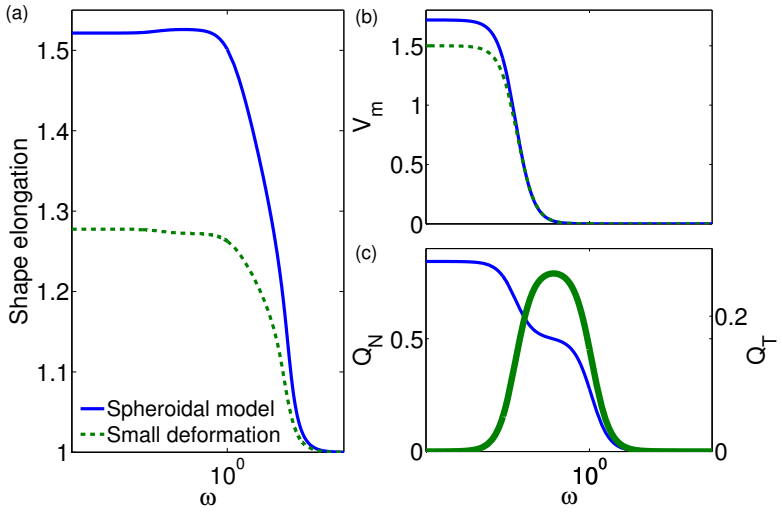

FIG. 3. Equilibrium deformation versus frequency ω for a prolate vesicle with $\sigma_r = 1.5$; $Ca_E = 6837$ and $s_0 = 1$. In (a) and (b), solid curves are from the spheroidal model and dashed curves are from the small-deformation model. (c) Normal (thin curve) and tangential (thick curve) electric stresses from the spheroidal model (equation 30 and equation 31).

by equations A1- A11 for the prolate shape, and equations A13- A23 for the oblate shape. Setting $\frac{d\chi}{dt} = 0$ the steady-state equilibrium shape is obtained by solving the non-linear equation:

$$\mathcal{Q}_N f_{21} + \mathcal{Q}_T \frac{f_{11}\left(\mu_r f_{22} + f_{23}\right)}{\mu_r f_{14} + f_{15}} = Ca_E^{-1}\left(\sigma_h f_{24} + f_\kappa\right). \tag{32}$$

Equation 32 shows that an equilibrium shape is achieved when the electric forces (on the left) are balanced by the tension and bending forces (on the right).

III. RESULTS

A. Comparison with small-deformation theory

The shape elongation $a/b = \xi_0/\sqrt{\xi_0^2 - 1}$ for prolate while $a/b = \lambda_0/\sqrt{\lambda_0^2 + 1}$ for oblate. Figure 3(a) shows the equilibrium shape elongation from the spheroidal model (solid lines) and the small-deformation theory[22] (dashed lines) for $\sigma_r = 1.5$, $Ca_E = 6837$ and $s_0 = 1$. We found that, for the same membrane tension s_0, the spheroidal model predicts larger deformation than the small deformation theory at a given frequency. The corresponding transmembrane potential magnitude V_m and the electric stresses (the normal component Q_N and the tangential component Q_T) are shown in figure 3(b) and (c), respectively. As we expect from § II A, the membrane potential from the spheroidal model is higher at low frequencies. The decrease in membrane potential at $\omega \approx 5 \times 10^{-3}$ in (b) coincides with an increase in the tangential electric stress, and a decrease in the electric pressure in (c).

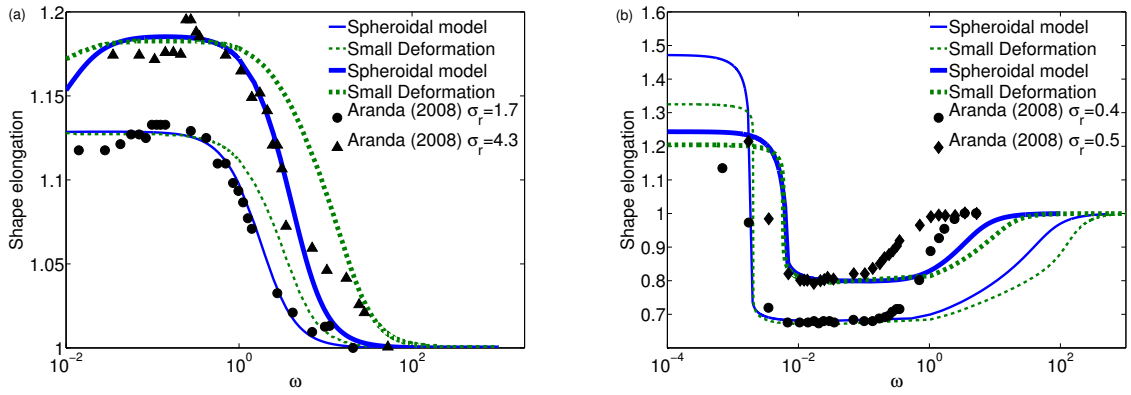

FIG. 4. Comparison between the experimental data of Aranda *et al.* [4] (symbols), the small deformation theory (dashed curves), and the current model (solid curves). (a) $\sigma_r > 1$; (b) $\sigma_r < 1$.

Experiment	s_0 used in spheroidal model	s_0 used in small-deformation model
$\sigma_r = 4.3$, $r_0 = 21.6\mu$m	43000	3000
$\sigma_r = 1.7$, $r_0 = 27.5\mu$m	80000	20000
$\sigma_r \approx 1$ (Pr), $r_0 = 27.5\mu$m	1000	1
$\sigma_r \approx 1$ (Ob), $r_0 = 37.5\mu$m	10^{-6}	10^{-7}
$\sigma_r = 0.5$, $r_0 = 12.8\mu$m	1000	100
$\sigma_r = 0.4$, $r_0 = 27.2\mu$m	70	1

TABLE I. Fitted values of $s_0 = \bar{\sigma}_0 r_0^2/\kappa$ for the experimental data in[4] with $\varepsilon_r = 1$, $\mu_r = 1$, $\kappa = 10 k_B T$ and $E_0 = 0.2$ kV/cm.

B. Comparison with Experiment

1. *Equilibrium shape elongation versus frequency*

Experiments[4] show that the equilibrium vesicle shape is spherical at very high frequencies ($\omega > 10^3$), where and the transmembrane potential is zero. At moderate frequencies ($\omega < 10^2$) the equilibrium vesicle shape can be prolate if $\sigma_r > 1$ or oblate if $\sigma_r < 1$. In particular, the equilibrium oblate vesicle for $\sigma_r < 1$ crosses over to the prolate equilibrium shape for $\omega < 10^{-2}$. These experimental findings are summarized (symbols) in figure 4 and figure 5, where we also compare between the spheroidal model (solid lines) and the small-deformation model[22] (broken lines). Following the approach in[22] we use s_0 as a fitting parameter (see Table I) and fix the bending stiffness $\kappa = 10 k_B T$. s_0 used in the spheroidal model is at least an order of magnitude larger than in small deformation. Nevertheless, they are comparable to values reported in previous work[24].

Figure 4(a) is for $\sigma_r > 1$ ('transition' *(1)* in[4]) where the equilibrium vesicle shape elongation is always greater (prolate) or equal (spherical) to one. We observe better agreement

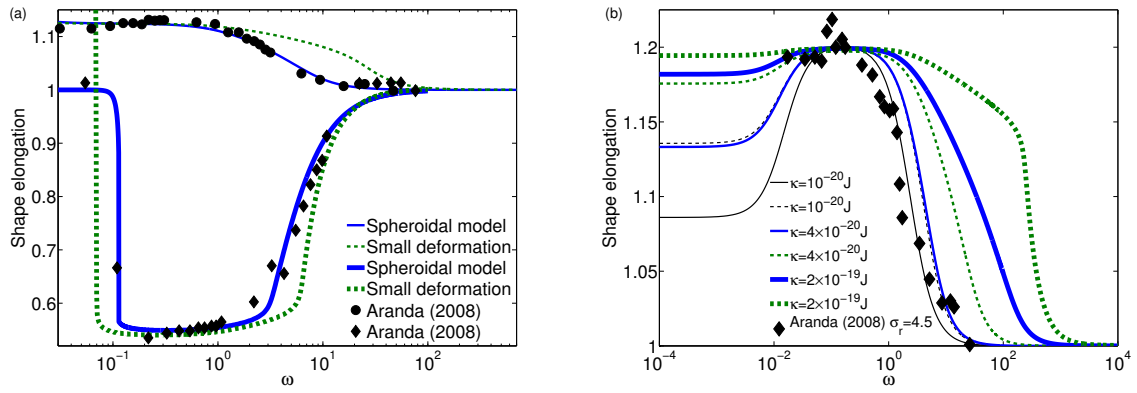

FIG. 5. Comparison between the experimental data of Aranda *et al.* [4] (symbols), the small deformation theory (dashed curves), and the spheroidal model (solid curve). (a) $\sigma_r \approx 1$. (b) $\sigma_r = 4.5$.

from the spheroidal model for $\sigma_r = 1.7$, while for $\sigma_r = 4.3$ the spheroidal results are in better agreement except for $\omega > 10$. Figure 4(b) is for $\sigma_r < 1$ ('transition' *(4)* in[4]) were the equilibrium vesicle shape can cross over from spherical at high frequencies $\omega > 20$ to oblate at intermediate frequencies $\sim 3 \times 10^{-3} \leq \omega \leq \sim 1$, and to prolate at low frequencies $10^{-4} \leq \omega \leq \sim 3 \times 10^{-3}$. In this case neither model agrees with the experiments for $1 > \omega > 0.5$, where the equilibrium vesicle shape crosses over from oblate to spherical as ω increases.

In 'transition' *(3)* of[4] where σ_r is close to unity, the value of σ_r determines the shape of the vesicles: Prolate for $\sigma_r > 1$ and oblate for $\sigma_r < 1$. Figure 5(a) shows the comparison between models and experiments for $\sigma_r \approx 1$. Next we focus on the effect of bending rigidity on the equilibrium vesicle shape. For experiments in[4], the bending stiffness varies between 4×10^{-20} J[24] and 2.3×10^{-19} J[43]. In addition, recent measurements on SOPC bilayer membranes[44] yielded a bending stiffness as low as 7×10^{-21} J. Figure 5(b) shows a comparison between theories and experiments for $\sigma_r = 4.5$ and with various values of the bending stiffness. Both theories are very sensitive to changes in the bending stiffness: We found good agreement with experiments up to $\kappa = 4 \times 10^{-20}$ J for the spheroidal model, and up to $\kappa = 10^{-20}$ J for the small deformation. Beyond these values, the two models overestimate the deformation.

Vesicles take various equilibrium shapes at different frequencies and conductivity ratios. Aranda *et al.* [4] constructed a morphological diagram on the $\omega - \sigma_r$ plane by performing a series of experiments using over 60 vesicles ranging $4 - 50\mu$m in size. Fixing the conductivity inside the vesicles and varying the conductivity of the external fluid phase, they subjected the vesicles to an AC field at a frequency ranging between ≈ 2 kHz $-$ 20 MHz.

Figure 6 shows the shape variations in the $\omega - \sigma_r$ plane. The experimental data points indicate the value at which the vesicle changes shape as frequency increases. Figure 6 also compares the predictions from the spheroidal model, the small deformation theory and the result using the energy minimization approach[17]. The spheroidal and small deformation models give agreements with experiments: The prolate-to-oblate and prolate-to-sphere fre-

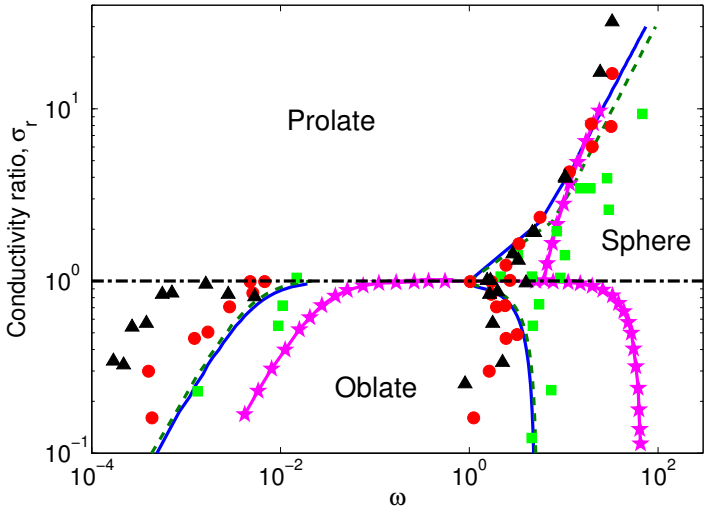

FIG. 6. Morphological phase diagram for $\kappa = 10k_BT$, $E_0 = 2 \times 10^4$ V/m. The conductivity ratio σ_r is determined by varying the conductivity of the external medium (σ_e) and holding the interior fixed at $\sigma_i = 15\mu$S/cm (□), 65μS/cm (◯), 130μS/cm (△). Solid lines are from the spheroidal model with $s_0 = 45000$, dashed lines are from the small-deformation model with $s_0 = 10000$, and the starred-solid lines are from the energy minimization approach[17].

quencies increase with σ_r, while the oblate-to-sphere frequencies decrease with increasing σ_r. The surface energy minimization model in[17] (starred-solid lines) only gives qualitative agreement with experiments.

2. *Prolate-to-oblate crossover frequency*

The frequency at which the equilibrium vesicle shape crosses over from prolate to oblate depends on the conductivity ratio and vesicles size[4,17,45–47]. In a recent experiment Peterlin[17] put vesicles of different sizes under a sequence of step-wise frequency changes, ranging from hundreds to a thousand hertz for a duration of ≈ 3 secs with the frequency increasing or decreasing around the crossover frequency, see the symbols in figure 7(a).

At the crossover frequency (from prolate to oblate, for example), the equilibrium vesicle shape is spherical, which corresponds to the limit $\xi \to \infty$, $\Delta \approx 0$, and V_m reduces to spherical shell potential. This allows us to perform an asymptotic analysis on the equilibrium vesicle shape elongation near the crossover frequency, where we expand all functions of ξ in terms of $1/\epsilon^2$ with $\epsilon \ll 1$. For example, the Legendre polynomial $Q_1(\xi)$ and its derivative take the form $Q_1 \sim \frac{1}{3\xi^2} + \frac{1}{5\xi^4} + \mathcal{O}\left(\frac{1}{\xi^6}\right)$, $Q_1' \sim -\frac{2}{3\xi^3} - \frac{4}{5\xi^5} + \mathcal{O}\left(\frac{1}{\xi^7}\right)$. We expand the semi-focal length $c \sim \frac{1}{\xi} + \mathcal{O}\left(\frac{1}{\xi^3}\right)$, and similarly for all the other functions in Appendix A. We then substitut these expansions into equations 16, 30 and 32, and obtain an equation expanded in

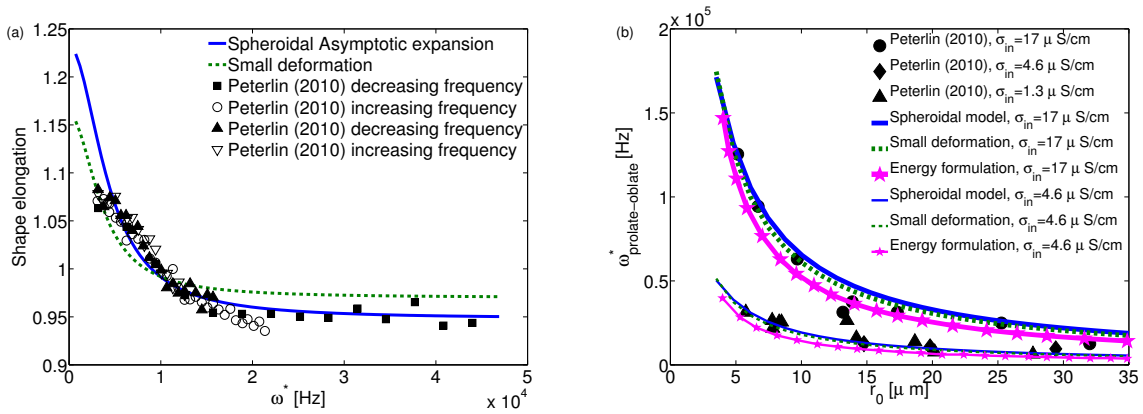

FIG. 7. (a) Shape elongation near the crossover between prolate and oblate for $\sigma_r = 0.9$, $d = 4$ nm, $\kappa = 1.2\times10^{-19}$ J, and $E_0 = 500$ V/m. Symbols are the experimental data in[17]: Full (open) symbols are with increasing (decreasing) frequency. $s_0 = 1$ is used in both spheroidal and small-deformation models. (b) Prolate-oblate crossover frequency, ω^* as a function of vesicle radius r_0.

$1/\xi_0 \sum_{n=0} a_n \xi_0^{-2n} = 0$, where the coefficients a_n are functions of fluid and membrane properties. Keeping all the leading-order terms at $\mathcal{O}(1/\xi_0^2)$ we obtain an equation for ξ_0^2, which gives the solution

$$\xi_0(\omega) = \sqrt{\frac{2}{35}} \frac{\sqrt{-Ca_E ABC}}{G} \tag{33}$$

with coefficients A, B, C and G given in Appendix D. The leading-order shape elongation for a prolate vesicle near the crossover frequency is $\frac{a}{b} \sim 1 + \frac{1}{2\xi_0^2} + \mathcal{O}\left(\frac{1}{\xi_0^4}\right)$. Similarly for the crossover from oblate to prolate, the leading order shape elongation would be $\frac{a}{b} \sim 1 - \frac{1}{2\lambda_0^2} + \mathcal{O}\left(\frac{1}{\lambda_0^4}\right)$.

Figure 7(a) shows the comparison between the asymptotic analysis on the spheroidal model (solid line), calculation from the small deformation model (dashed line) and experiments (symbols). First of all, we observe a small difference in the crossover frequency (value of ω^* when shape elongation is unity) between the solid and the dashed lines: We attribute this small disagreement to the differences in treating the stress balance on the membrane between the two models. Secondly, we observe a significant difference in the slope at the crossover frequency between the two curves, with the spheroidal model in better agreement with the experimental data. We have tried to adjust s_0 to fit the small-deformation model to experimental data with the same slope at the crossover frequency, but we are unable to find a reasonably good fit. The crossover frequency also depends on the initial spherical size of vesicles. Figure 7(b) shows the comparison results of the experiment in[17], where the spheroidal results (solid curves), the small-deformation results (dashed curves) and the energy-minimization results (starred solid curves) are all plotted against the initial spherical radius r_0. All three theories show good agreement with the experimental data.

IV. CONCLUSION

In this work we constructed a spheroidal model to study the equilibrium deformation of a vesicle under ac electric fields within the leaky dielectric framework. Such an approach has been shown to capture large equilibrium electro-deformation of a viscous surfactant-covered drop[38] and the transient dynamics of a vesicle in a dc field[23]. In our spheroidal model the vesicle membrane is modeled as a non-conducting capacitive elastic membrane with a homogeneous tension that depends on the excess area. We developed a spheroidal shell model to compute the potential across the vesicle membrane. By adjusting the membrane tension coefficient s_0, we are able to reproduce the experiments in terms of the dependence of the vesicle shape elongation on the frequency ω, conductivity ratio σ_r, and the initial spherical radius of the vesicle. We further explore the effects of bending rigidity on the shape elongation. In addition we conducted an asymptotic analysis on our spheroidal model around the prolate-oblate crossover frequency, and we find very good agreement with the experiments in terms of both the value of crossover frequency and the rate of change of shape elongation with respect to frequency.

In this work we did not consider effects of membrane conductance and displacement currents across the membrane, both of which are found to destabilize a planar membrane under electric fields[48–50]. We focus on the equilibrium deformation and ignore the time-dependent harmonic stresses. Consequently we did not consider the dynamic transient and oscillation around the averaged equilibria, yet our spheroidal model can easily incorporate the time-dependent stresses and this is now part of an ongoing work. In addition the vesicle area is not held constant in our model. Furthermore our spheroidal model is applicable only to spheroidal deformation, and cannot describe the dynamics and equilibrium shapes of an axi-symmetric non-spheroidal vesicle.

We are now refining our model by replacing the leaky dielectric fluids with electrolytes in the solvents, in which case the electric potential no longer satisfies the simple Laplace equation, but the Poisson-Boltzmann equations that take into account the transport of various charged species in the fluids. The solvents are known to destabilize lipid membrane under a dc electric field. It is reasonable to expect that much more complex dynamics and equilibrium shape for a vesicle immersed in electrolytes under an ac field. For example, depending on the net charges in the bulk, the vesicle may have very different morphology under an electric field. We are currently investigating how the morphological phase diagram in figure 6 may be altered by solvents.

ACKNOWLEDGMENTS

YNY acknowledge useful discussions with P. M Vlahovska and partial support from NSF grant DMS-1222550.

Appendix A: Integrals in the spheroidal model

The functions $f_{11}(\xi_0) - f_{15}(\xi_0)$ are given by

$$f_{11} = \int \frac{\eta G_3(\eta)}{\xi_0^2 - \eta^2} d\eta, \tag{A1}$$

$$f_{12} = \frac{1}{\xi_0^2 - 1} \int G_3(\eta) \left(\frac{2\eta G_3'(\eta)}{(\xi_0^2 - \eta^2)^2} + \frac{G_3''(\eta)}{\xi_0^2 - \eta^2} \right) d\eta, \tag{A2}$$

$$f_{13} = \frac{G_3' G_5'' - G_5' G_3''}{2N} f_{11}, \tag{A3}$$

$$f_{14} = -\xi_0 H_3' \int \frac{\eta G_3(\eta)}{(\xi_0^2 - \eta^2)^2} d\eta + \frac{H_3''}{2} f_{11}, \tag{A4}$$

$$f_{15} = \xi_0 H_3' \int \frac{\eta G_3(\eta)}{(\xi_0^2 - \eta^2)^2} d\eta - \frac{(G_3 G_5'' - G_5 G_3'') H_3'}{2N} f_{11}. \tag{A5}$$

Furthermore, the functions $f_{21}(\xi_0) - f_{26}(\xi_0)$ are given by

$$f_{21} = \frac{\xi_0^2}{2} \int \frac{(3\eta^2 - 1)(\eta^2 - 1)}{\xi_0^2 - \eta^2} d\eta, \tag{A6}$$

$$f_{22} = -H_3' \int \frac{(1 - 3\eta^2)(2\eta^4 + \xi_0^2 - 3\xi_0^2\eta^2)}{(\xi_0^2 - \eta^2)^2} d\eta + 3H_3 \xi_0 \int \frac{1 - 3\eta^2}{\xi_0^2 - \eta^2} d\eta, \tag{A7}$$

$$f_{23} = -\frac{49}{30N} G_3 H_3' (1 - 3\xi_0^2) + H_3' \int \frac{(1 - 3\eta^2)(2\eta^4 + \xi_0^2 - 3\xi_0^2\eta^2)}{(\xi_0^2 - \eta^2)^2} d\eta, \tag{A8}$$

$$f_{24} = \frac{1}{c} \left[\xi_0 (\xi_0^2 - 1)^{1/2} \int \frac{\gamma\,(3\eta^2 - 1)}{(\xi_0^2 - \eta^2)^{3/2}} d\eta + \frac{\xi_0}{(\xi_0^2 - 1)^{1/2}} \int \frac{\gamma\,(3\eta^2 - 1)}{(\xi_0^2 - \eta^2)^{1/2}} d\eta \right], \tag{A9}$$

$$f_{25} = -\frac{\xi_0}{\xi_0^2 - 1} \int \frac{(1 - 3\eta^2)(2\xi_0^2 - \eta^2 - 1) G_3'(\eta)}{(\xi_0^2 - \eta^2)^2} d\eta + 3\xi_0 \int \frac{1 - 3\eta^2}{\xi_0^2 - \eta^2} d\eta - \frac{(\mu_r - 1) f_{12} + f_{13}}{\mu_r f_{14} + f_{15}} f_{22}, \tag{A10}$$

$$f_{26} = \frac{\xi_0}{\xi_0^2 - 1} \int \frac{(1 - 3\eta^2)(2\xi_0^2 - \eta^2 - 1) G_3'(\eta)}{(\xi_0^2 - \eta^2)^2} d\eta - \frac{49}{30N} (1 - 3\xi_0^2) G_3' - \frac{(\mu_r - 1) f_{12} + f_{13}}{\mu_r f_{14} + f_{15}} f_{22}, \tag{A11}$$

$$f_\kappa = \frac{-72 + 106\xi_0^2 - 225\xi_0^4 + 135\xi_0^6 + 45\xi_0^4 (4 - 3\xi_0^2) \sqrt{\xi_0^2 - 1}\, \mathrm{arccsc}(\xi_0)}{15 c^3 \xi_0^3(\xi_0^2 - 1)^2}. \tag{A12}$$

The functions $f_{11}(\lambda_0) - f_{15}(\lambda_0)$ in are given by

$$f_{11} = \int \frac{\eta G_3(\eta)}{\lambda_0^2 + \eta^2} d\eta, \tag{A13}$$

$$f_{12} = \frac{1}{\lambda_0^2 + 1} \int G_3(\eta) \left(\frac{-2\eta G_3'(\eta)}{(\lambda_0^2 + \eta^2)^2} + \frac{G_3''(\eta)}{\lambda_0^2 + \eta^2} \right) d\eta, \tag{A14}$$

$$f_{13} = \frac{G_3' G_5'' - G_5' G_3''}{2N} f_{11}, \tag{A15}$$

$$f_{14} = \lambda_0 H_3' \int \frac{\eta G_3(\eta)}{(\lambda_0^2 + \eta^2)^2} d\eta - \frac{H_3''}{2} f_{11}, \tag{A16}$$

$$f_{15} = -\lambda_0 H_3' \int \frac{\eta G_3(\eta)}{(\lambda_0^2 + \eta^2)^2} d\eta + \frac{(G_3 G_5'' - G_5 G_3'') H_3'}{2N} f_{11}. \tag{A17}$$

Furthermore, the functions $f_{21}(\lambda_0) - f_{26}(\lambda_0)$ are given by

$$f_{21} = \frac{\lambda_0^2}{2} \int \frac{(3\eta^2 - 1)(\eta^2 - 1)}{\lambda_0^2 + \eta^2} d\eta, \tag{A18}$$

$$f_{22} = H_3' \int \frac{(3\eta^2 - 1)(\lambda_0^2 - 3\lambda_0^2 \eta^2 - 2\eta^4)}{(\lambda_0^2 + \eta^2)^2} d\eta + 3\lambda H_3 \int \frac{3\eta^2 - 1}{\lambda_0^2 + \eta^2} d\eta \tag{A19}$$

$$f_{23} = -H_3' \int \frac{(3\eta^2 - 1)(\lambda_0^2 - 3\lambda_0^2 \eta^2 - 2\eta^4)}{(\lambda_0^2 + \eta^2)^2} d\eta + \frac{49}{30N} (1 + 3\lambda_0^2) g_3 H_3', \tag{A20}$$

$$f_{24} = \frac{1}{c} \left[\lambda_0 (\lambda_0^2 + 1)^{1/2} \int \frac{\gamma\,(1 - 3\eta^2)}{(\lambda_0^2 + \eta^2)^{3/2}} d\eta + \frac{\lambda_0}{(\lambda_0^2 + 1)^{1/2}} \int \frac{\gamma\,(1 - 3\eta^2)}{(\lambda_0^2 + \eta^2)^{1/2}} d\eta \right], \tag{A21}$$

$$f_{25} = \frac{\lambda_0}{\lambda_0^2 + 1} \int \frac{(3\eta^2 - 1)(2\lambda_0^2 + \eta^2 + 1) G_3'(\eta)}{(\lambda_0^2 + \eta^2)^2} d\eta + 3\lambda \int \frac{3\eta^2 - 1}{\lambda_0^2 + \eta^2} d\eta + \frac{(\mu_r - 1) f_{12} + f_{13}}{\mu_r f_{14} + f_{15}} f_{22}, \tag{A22}$$

$$f_{26} = -\frac{\lambda_0}{\lambda_0^2 + 1} \int \frac{(3\eta^2 - 1)(2\lambda_0^2 + \eta^2 + 1) G_3'(\eta)}{(\lambda_0^2 + \eta^2)^2} d\eta + \frac{49}{30N} (1 + 3\lambda_0^2) g_3' + \frac{(\mu_r - 1) f_{12} + f_{13}}{\mu_r f_{14} + f_{15}} f_{23}, \tag{A23}$$

$$f_\kappa = \frac{72 + 106\lambda_0^2 + 225\lambda_0^4 + 135\lambda_0^6 - 45\lambda_0^4 (4 + 3\lambda_0^2) \sqrt{\lambda_0^2 + 1}\, \mathrm{arccoth}(\sqrt{\lambda_0^2 + 1})}{15 c^3 \lambda_0^3 (\lambda_0^2 + 1)^2}. \tag{A24}$$

Appendix B: Transmembrane Potential

The electric potential coefficients $\beta_e,\ \alpha_m,\ \beta_m,\ \alpha_i$ are obtained from the boundary conditions at $\xi = \xi_e$ and $\xi = \xi_i$ (see Figure 1):

(a) Continuity of the potential:

$$\phi_e(\xi_e) = \phi_m(\xi_e), \quad \phi_m(\xi_i) = \phi_i(\xi_i), \tag{B1}$$

(b) Continuity of the normal component of the complex current density, equation 9:

$$-\frac{K_e}{h_\xi}\frac{\partial\phi_e}{\partial\xi}\bigg|_{\xi_e} = -\frac{K_m}{h_\xi}\frac{\partial\phi_m}{\partial\xi}\bigg|_{\xi_e}, \quad -\frac{K_m}{h_\xi}\frac{\partial\phi_m}{\partial\xi}\bigg|_{\xi_i} = -\frac{K_i}{h_\xi}\frac{\partial\phi_i}{\partial\xi}\bigg|_{\xi_i}. \tag{B2}$$

Condition a is justified because the normal component of the electric field must be bounded[19,27].

The remaining electric potential coefficients are given by:

$$\alpha_i = \frac{cK_eK_m\left(\xi_iQ_i' - Q_i\right)\left(Q_e - \xi_eQ_e'\right)}{D(\omega)}, \tag{B3}$$

$$\alpha_m = \frac{cK_e\left(\xi_eQ_e' - Q_e\right)\left(K_iQ_i - K_m\xi_iQ_i'\right)}{D(\omega)}, \tag{B4}$$

$$\beta_m = \frac{c\xi_iK_e\left(K_i - K_m\right)\left(Q_e - \xi_eQ_e'\right)}{D(\omega)}, \tag{B5}$$

$$\begin{aligned}\beta_e = &\frac{c\xi_iK_e\left(K_i - K_m\right)Q_e}{D(\omega)} \\ &+ \frac{c\xi_e\left(K_i(K_m - K_e)Q_i + K_m\xi_i((K_m - K_i)Q_e' + (K_e - K_m)Q_i')\right)}{D(\omega)},\end{aligned} \tag{B6}$$

where

$$\begin{aligned}D(\omega) = &K_e\xi_eQ_e'\left(-K_iQ_i + K_m\xi_iQ_i'\right) \\ &+Q_e\left(K_iK_mQ_i + (K_e - K_m)(K_i - K_m)\xi_iQ_e' - \xi_iQ_i'K_m^2\right),\end{aligned} \tag{B7}$$

and $Q_e \equiv Q_1(\xi_e), Q_i \equiv Q_1(\xi_i), Q_e' \equiv Q_1'(\xi_e), Q_i' \equiv Q_1'(\xi_i)$.

Appendix C: Maxwell stresses

The Maxwell stresses in prolate coordinates are given by

$$\begin{aligned}[\![\mathbf{S}_{\xi\xi}]\!] = \frac{1}{4c^2}\Bigg\{&\frac{\eta^2\left(\xi_0^2 - 1\right)}{\xi_0^2 - \eta^2}\left(c^2 - 2c\tau_3Q_1' + \left(\tau_3^2 + \tau_4^2\right)\left(Q_1'\right)^2\right) \\ &+\frac{\xi_0^2\left(\eta^2 - 1\right)}{\xi_0^2 - \eta^2}\left(c^2 - \frac{2c\tau_3Q_1}{\xi_0} + \left(\tau_3^2 + \tau_4^2\right)\left(\frac{Q_1}{\xi_0}\right)^2\right) \\ &-\frac{\left(\tau_1^2 + \tau_2^2\right)}{\epsilon_r}\left(\frac{\eta^2\left(\xi_0^2 - 1\right)}{\xi_0^2 - \eta^2} + \frac{\xi_0^2\left(\eta^2 - 1\right)}{\xi_0^2 - \eta^2}\right)\Bigg\},\end{aligned} \tag{C1}$$

and

$$\begin{aligned}[\![\mathbf{S}_{\xi\eta}]\!] = \frac{\eta}{2c^2}\frac{\sqrt{\left(\xi_0^2 - 1\right)\left(1 - \eta^2\right)}}{\xi_0^2 - \eta^2}\Big\{&\left(c^2\xi_0 - c(Q_1 + \xi_0Q_1')\tau_3 + \left(\tau_3^2 + \tau_4^2\right)Q_1Q_1'\right) \\ &- \left(\tau_1^2 + \tau_2^2\right)\xi_0/\epsilon_r\Big\},\end{aligned} \tag{C2}$$

where $\tau_1 = \Re[\beta]$, $\tau_2 = \Im[\beta]$, $\tau_3 = \Re[\alpha]$, and $\tau_4 = \Im[\alpha]$. $\Re[\ ]$ and $\Im[\ ]$ denote the real and imaginary parts.

The equivalent equations in the oblate coordinates are

$$[\![\mathbf{S}_{\lambda\lambda}]\!] = \frac{1}{4c^2}\left\{\frac{\eta^2\left(\lambda_0^2+1\right)}{\lambda_0^2+\eta^2}\left(c^2 - 2c\tau_3 Q_1' + \left(\tau_3^2+\tau_4^2\right)\left(Q_1'\right)^2\right)\right.$$
$$+\frac{\lambda_0^2\left(\eta^2-1\right)}{\lambda_0^2+\eta^2}\left(c^2 - \frac{2c\tau_3 Q_1}{\lambda_0} + \left(\tau_3^2+\tau_4^2\right)\left(\frac{Q_1}{\lambda_0}\right)^2\right)$$
$$\left.-\frac{\left(\tau_1^2+\tau_2^2\right)}{\epsilon_r}\left(\frac{\eta^2\left(\lambda_0^2+1\right)}{\lambda_0^2+\eta^2} + \frac{\lambda_0^2\left(\eta^2-1\right)}{\lambda_0^2+\eta^2}\right)\right\}, \tag{C3}$$

and

$$[\![\mathbf{S}_{\lambda\eta}]\!] = \frac{\eta}{2c^2}\frac{\sqrt{\left(\lambda_0^2+1\right)\left(1-\eta^2\right)}}{\lambda_0^2+\eta^2}\left\{\left(c^2\lambda_0 - c(Q_1+\lambda_0 Q_1')\tau_3 + \left(\tau_3^2+\tau_4^2\right)Q_1 Q_1'\right)\right.$$
$$\left.-\left(\tau_1^2+\tau_2^2\right)\lambda_0/\epsilon_r\right\}. \tag{C4}$$

Appendix D: Asymptotic analysis

$$A = (2+\sigma_r)^2 + 9\omega^2, \tag{D1}$$
$$B = 2\sigma_r^2(2+\sigma_r)^2 + \left(18\sigma_r^2 + C_m^2(\sigma_r-1)(2+\sigma_r)^2(5+2\sigma_r) + 2C_m\sigma_r(\sigma_r+\sigma_r^2-2)\right)\omega^2, \tag{D2}$$
$$C = -2\sigma_r^2(2+\sigma_r)^3\left(9Ca_E(19+13\sigma_r) + 560(2+\sigma_r)(4+s_0)\right) - 71680C_m^2\omega^2 \tag{D3}$$
$$+(9Ca_E(2+\sigma_r)\left(-6\sigma_r^2(121+71\sigma_r) + C_m(\sigma_r-1)\sigma_r(2+\sigma_r)(130+107\sigma_r)\right.$$
$$\left.+C_m^2(60+23\sigma_r)(\sigma_r+\sigma_r^2-2)^2\right) + 280\left(-72\sigma_r^2(2+\sigma_r)^2(4+s_0)\right.$$
$$\left.+C_m^2\left(-64s_0 - \sigma_r(4+\sigma_r)(4+\sigma_r(2+\sigma_r))(12+\sigma_r(6+\sigma_r))(4+s_0)\right)\right))\omega^2$$
$$-9(-711Ca_E C_m\sigma_r(\sigma_r+\sigma_r^2-2) + 288\sigma_r^2\left(6Ca_E + 35(4+s_0)\right)$$
$$+5C_m^2(2+\sigma_r)^2(9Ca_E(\sigma_r-1)^2 + 112(2+\sigma_r)^2(4+s_0)))\omega^4$$
$$-22680C_m^2(2+\sigma_r)^2(4+s_0)\omega^6,$$
$$G = 3Ca_E\left((2+\sigma_r)^2+9\omega^2\right)\left(2\sigma_r^2(2+\sigma_r)^2 + \left(18\sigma_r^2 + C_m^2(\sigma_r-1)(2+\sigma_r)^2(5+2\sigma_r)\right.\right. \tag{D4}$$
$$\left.\left.+2C_m\sigma_r(\sigma_r+\sigma_r^2-2)\right)\omega^2\right).$$

---

[1] K. A. Riske and R. Dimova, "Electro-deformation and poration of giant vesicles viewed with high temporal resolution," Biophys. J., **88**, 1143–1155 (2005).

[2] K. A. Riske and R. Dimova, "Electric pulses induce cylindrical deformations on giant vesicles in salt solutions," Biophys. J., **91**, 1778–1786 (2006).

[3] R. Dimova, K. A. Riske, S. Aranda, N. Bezlyepkina, R. L. Knorr, and R. Lipowsky, "Giant vesicles in electric fields," Soft Matter, **3**, 817–827 (2007).

[4] S. Aranda, K. A. Riske, R. Lipowsky, and R. Dimova, "Morphological transitions of vesicles induced by alternating electric fields," Biophys. J.: Biophys. Lett., L19 (2008).

[5] E. Neumann, A. E. Sowers, and C. A. Jordan, *Electroporation and electrofusion in cell biology* (Plenum, New York, 1989).

[6] D. C. Chang, B. M. Chassey, J. A. Saunders, and A. E. Sowers, *Guide to electroporation and electrofusion* (Academic Press, New York, 1992).

[7] U. Zimmermann and G. A. Neil, *Electromanipulation of cells* (CRC Press, Boca Raton, FL, 1996).

[8] W. Sung and P. J. Park, "Dynamics of pore growth in membranes and membrane stability," Biophys. J., **73**, 1797–1804 (1997).

[9] J. C. Neu and W. Krassowska, "Asymptotic model of electroporation," Phys. Rev. E, **59**, 3471–3482 (1999).

[10] K. C. Smith, J. C. Neu, and W. Krassowska, "Model of creation and evolution of stable electrophorus for DNA delivery," Biophys. J., **86**, 2813–2826 (2004).

[11] W. Krassowska and P. D. Filev, "Modeling electroporation in a single cell," Biophys. J., **92**, 404–417 (2011).

[12] J. Teissié, J. M. Escoffre, M. P. Rols, and M. Golzio, "Time dependence of electric field effects on cell membranes. a review for a critical selection of pulse duration for therapeutical applications," Radiol. Oncol., **42**, 196–206 (2008).

[13] T. Portet, C. Mauroy, V. Démery, T. Houles, J.-M. Escoffre, D. S. Dean, and M.-P. Rols, "Destabilizing giant vesicles with electric fields: An overview of current applications," J. Membrane Biol., **245**, 555–564 (2012).

[14] P. F. Salipante, R. Knorr, R. Dimova, and P. M. Vlahovska, "Electrodeformation method for measuring the capacitance of bilayer membranes," Soft Matter, **8**, 3810–3816 (2012).

[15] W. Helfrich, "Deformation of lipid bilayer spheres by electric fields," Z. Naturforsch, **29c**, 182–183 (1974).

[16] M. Winterhalter and W. Helfrich, "Deformation of spherical vesicles by electric fields," J. Coll. Int. Sci., **122**, 583–586 (1988).

[17] P. Peterlin, "Frequency-dependent electrodeformation of giant phospholipid vesicles in ac electric field," J. Biol. Phys., **36**, 339–354 (2010).

[18] T. Yamamoto, S. Aranda-Espinoza, R. Dimova, and R. Lipowsky, "Stability of spherical vesicles in electric fields," Langmuir, **26**, 12390–12407 (2010).

[19] H. Hyuga, K. Kinosita Jr., and N. Wakabayashi, "Transient and steady-state deformations of a vesicle with an insulating membrane in response to step-function or alternating electric fields," Jpn. J App. Phys., **30**, 2649–2656 (1991).

[20] H. Hyuga, K. Kinosita Jr., and N. Wakabayashi, "Deformation of vesicles under the influence of strong electric fields," Jpn. J App. Phys., **30**, 1141–1148 (1991).

[21] M. M. Sadik, J. Li, J. W. Shan, D. I. Shreiber, and H. Lin, "Vesicle deformation and poration under strong dc electric fields," Phys. Rev. E, **83**, 066316 (2011).

[22] P. M. Vlahovska, R. S. Graciá, S. Aranda-Espinoza, and R. Dimova, "Electrohydrodynamic model of vesicle deformation in alternating electric fields," Biophys. J., **96**, 4789 (2009).

[23] J. Zhang, J. D. Zahn, W. Tan, and H. Lin, "A transient solution for vesicle electrodeformation and relaxation," Phys. Fluids, **25**, 071903 (2013).

[24] M. Kummrow and W. Helfrich, "Deformation of giant lipid vesicles by electric fields," Phys.

Rev. E, **44**, 8356–8360 (1991).

[25] P. Marszalek, D.-S. Liu, and T. Y. Tsong, "Schwan equation and transmembrane potential induced by alternating electric field," Biophys. J., **58**, 1053–1058 (1990).

[26] I. Turcu and C. M. Lucaciu, "Dielectrophoresis: a spherical shell model," J. Phys. A: Math. Gen., **22**, 985–993 (1989).

[27] C. Grosse and H. P. Schwan, "Cellular membrane potentials induced by alternating fields," Biophys. J., **63**, 1632 (1992).

[28] K. A. DeBruin and W. Krassowska, "Modeling electroporation in a single cell. i. effects of field strength and rest potential," Biophys. J., **77**, 1213–1224 (1999).

[29] K. Maswiwat, D. Wachner, R. Warnke, and J. Gimsa, "Simplified equations for the transmembrane potential induced in ellipsoidal cells of rotational symmetry," J. Phys. D: Appl. Phys., **40**, 914–923 (2007).

[30] G. Bryant and J. Wolfe, "Electromechanical stresses produced in the plasma membranes of suspended cells by applied electric fields," J. Membr. Biol., **96**, 129–139 (2008).

[31] R. A. Jerry, A. S. Popel, and W. E. Brownell, "Potential distribution for a spheroidal cell having a conductive membrane in an electric field," IEEE Trans. Biomed. Eng., **43**, 970 (1996).

[32] M. Klee and R. Plonsey, "Finite difference solution for biopotentials of axially symmetric cells," Biophys. J., **12**, 1661–1675 (1972).

[33] J. Gimsa and D. Wachner, "A polarization model overcoming the geometric restrictions of the laplace solution for spheroidal cells: obtaining new equations for field-induced forces and transmembrane potential," Biophys. J., **77**, 1316 (1999).

[34] K. Maswiwat, D. Wachner, and J. Gimsa, "Effects of cell orientation and electric field frequency on the transmembrane potential induced in ellipsoidal cells," Bioelectrochemistry, **74**, 130–141 (2008).

[35] T. Kotnik and D. Miklavčič, "Analytical description of transmembrane voltage induced by electric fields on spheroidal cells," Biophys. J., **79**, 670–679 (2000).

[36] N. Bentenitis and S. Krause, "Droplet deformation in DC electric fields: The extended leaky dielectric model," Langmuir, **21**, 6194–6209 (2005).

[37] J. Zhang, J. Zahn, and H. Lin, "A transient solution for deformation under electric fields I: Droplets," Phys. Rev. E, **87**, 043008 (2013).

[38] H. Nganguia, Y.-N. Young, P. M. Vlahovska, J. Bławzdziewcz, J. Zhang, and H. Lin, "Equilibrium electroc-deformation of a surfactant-laden viscous drop," Phys. Fluids, **accepted** (2013).

[39] X. Wang, X.-B. Wang, and P. R. C. Gascoyne, "General expressions for dielectrophoretic force and electrorotational torque derived using the maxwell stress tensor method," J. Electrostatics, **39**, 277 (1997).

[40] G. Dassios, M. Hadjinicolaou, and A. C. Payatakes, "Generalized eigenfunctions and complete semi separable solutions for stokes flow in spheroidal coordinates," Quat. App. Math., **52**, 157–191 (1994).

[41] G. Dassios, M. Hadjinicolaou, F. A. Coutelieris, and A. C. Payatakes, "Stokes flow in spheroidal particle-in-cell models with Happel and Kuwabara boundary conditions," Int. J. Engng Sci., **33**, 1465–1490 (1995).

[42] S. Chandrasekhar, *Hydrodynamic and hydromagnetic stability* (Dover Publications, INC, New

York, 1981).

[43] R. M. Servuss, V. Harbich, and W. Helfrich, "Measurements of the curvature-elastic modulus of egg lecithin bilayers," Biochem. Biophys. Acta, **436**, 900–903 (1976).

[44] G. Popescu, T. Ikeda, K. Goda, C. A. Best-Popescu, M. Laposata, S. Manley, R. R. Dasari, K. Badizadegan, and M. S. Feld, "Optical measurement of cell membrane tension," Phys. Rev. Lett., **97**, 218101 (2006).

[45] M. D. Mitov, P. Méléard, M. Winterhalter, M. I. Angelova, and P. Bothorel, "Electric-field-dependent thermal fluctuations of giant vesicles," Phys. Rev. E, **48**, 628–631 (1993).

[46] P. Peterlin, S. Svetina, and B. Zeks, "The prolate-to-oblate shape transition of phospholipid vesicles in response to frequency variation of an ac electric field can be explained by the dielectric anisotropy of a phospholipid bilayer," J. Phys. Condens. Matter, **19**, 136220 (2007).

[47] K. Antonova, V. Vitkova, and M. D. Mitov, "Deformation of giant vesicles in ac electric fields –dependence of the prolate-to-oblate transition frequency on vesicle radius," EPL, **89**, 38004 (2010).

[48] J. Schwalbe, P. M. Vlahovska, and M. Miksis, "Vesicle electrohydrodynamics," Phys. Rev. E, **83**, 046309 (2011).

[49] J. Seiwert and P. M. Vlahovska, Phys. Rev. E, **87**, 022713 (2013).

[50] Y.-N. Young, S. Veerapaneni, and M. Miksis, Phys. Fluids, **submitted** (2013).